Multiscale Variability of the River Runoff System in China and Its Long-Term Link to Precipitation and Sea Surface Temperature

YONGKANG XUE,*,+ SHUFEN SUN,# K.-M. LAU,@ JINJUN JI,*,+ ISABELLE POCCARD,* RENHE ZHANG,&
HYUN-SUK KANG,* GUOXIONG WU,# JOHN C. SCHAAKE,** JIAN YUN ZHANG,++ YANJUN JIAO##

*Department of Geography, University of California, Los Angeles, Los Angeles, California
+Department of Atmospheric and Oceanic Sciences, University of California, Los Angeles, Los Angeles, California
#LASG, Institute of Atmospheric Physics, Beijing, China
@NASA GSFC, Greenbelt, Maryland
&Chinese Academy of Meteorological Sciences, Beijing, China
**NOAA/NWS, Silver Spring, Maryland
++Ministry of Hydraulic Engineering and Water Resources, Beijing, China
##University of Quebec at Montreal, Montreal, Quebec, Canada

(Manuscript received 1 December 2004, in final form 26 February 2005)

ABSTRACT

This is an exploratory study to investigate the spatial and temporal characteristics of east China's (EC) river runoff and their relationship with precipitation and sea surface temperature (SST) at the continental scale. Monthly mean data from 72 runoff stations and 160 precipitation stations in EC, covering a period between 1951 and 1983, are used for this study. The station river runoff data have been spatially interpolated onto 1° grid boxes as runoff depth based on an extracted drainage network. Comparing runoff depth with precipitation shows that seasonal variation in runoff is consistent with the development of the summer monsoon, including the delayed response of runoff in several subregions. The dominant spatial scales and temporal patterns of summer runoff and precipitation are studied with empirical orthogonal function (EOF) analysis and wavelet analyses. The analyses show interannual, biennial, and longer-term variations in the EOF modes. South–north dipole anomaly patterns for the first two runoff EOF's spatial distributions have been identified. The first/second runoff principal components (PCs) are highly correlated with the second/first precipitation PCs, respectively. The summer runoff's EOF PCs also show significant correlations with the multivariate El Niño–Southern Oscillation index (MEI) of the summer and winter months, while the summer precipitation PCs do not. Statistic analysis shows that EOF1 of runoff and EOF2 of precipitation are related to El Niño, while EOF2 of runoff and EOF1 of precipitation are related to a dipole SST anomaly over the northwestern Pacific. The interdecadal relationship between summer runoff, precipitation, and SST variability is further studied by singular value decomposition (SVD) analysis. Pronounced warming (SST) and drying (runoff) trends in first SVD PCs have been identified. These SVDs are used to reconstruct a decadal anomaly pattern, which produces flooding in part of the Chang Jiang River basin and dryness in the northern EC, consistent with observations.

1. Introduction

Detection of climate anomaly trends and discoveries of climate variability cycles are vital for the understanding of global climate change. Numerous studies have focused on investigating the climate variability of the earth system, in particular, the atmosphere–ocean system (e.g., Trenberth 1990; Lau and Weng 1999). However, the climate variability of ground hydrology at continental/global scales is still not adequately explored, with fewer reports (e.g., Lins 1985; Lettenmaier et al. 1994; Maurer et al. 2002). This study investigates the seasonal and interannual runoff variability in China at the continental scale and its relationship with precipitation, sea surface temperature (SST), and El Niño Southern Oscillation (ENSO) using river runoff and precipitation data that we obtained during the past few years.

The water cycle in East Asia exhibits very high spatial and temporal variability. Often, the amplitude of the interannual variability can be as large as the mean

Corresponding author address: Yongkang Xue, Department of Geography, University of California, Los Angeles, Los Angeles, CA 90095.
E-mail: yxue@geog.ucla.edu

state. Many studies (e.g., Lau 1992; Yatagai and Yasunari 1994; Nitta and Hu 1996; Weng et al. 1999, hereafter WLX99) have shown that observed precipitation exhibits strong interannual and interdecadal variations as well as a long-term dry trend in East Asia. Meanwhile, different climate anomaly signatures appear over different parts of China (e.g., Xue 1996), in particular, a dramatic shift from dry to wet conditions in central eastern China and an opposite shift in northern China in the late 1970s (WLX99). However, no comprehensive analyses have been conducted for river runoff resulting from the difficulty in data collection and the uniqueness of river runoff data. Unlike normal climate variables, river runoff is confined to river channels. Therefore, the techniques that are used for spatial interpolation of precipitation are not appropriate for river runoff data. Our study is motivated by the importance of the water cycle in East Asia and the lack of study on river runoff at the continental scale over the region.

2. Data and interpolation method

We have obtained monthly mean river runoff data from about 200 stations in China from different sources. These data are in hardcopy format and are mainly obtained from archives in China. In addition, data from 7 stations were obtained from the Global Runoff Data Center (GRDC), and data from 20 stations were obtained from the Ministry of Hydraulic Engineering and Water Resources of China. Although the runoff data from a few stations date back more than 100 yr, most of the stations only cover a short time period between 1951 and 1983. Because China changed its policy regarding the release of runoff data in 1983, we are unable to obtain data after 1983 for most parts of China. After eliminating station data with more than 1 yr missing between 1951 and 1983, a final 72 stations were selected for this study (Fig. 1a). The extracted data have a good spatial coverage of the eastern part of China, covering several basin areas except for the western parts of the Chang Jiang River (CJR) and Yellow River (YR) basins and the middle part of the Hai He River basin (Figs. 1a and 1b). A few isolated missing monthly data were either replaced by the average of the two nearest months or by the decadal monthly mean climatology. We have no quantitative information regarding the modulation of river runoff by reservoirs and irrigation, which are two major practices in modern Chinese water management (Nickum 1981). The possible implication of these effects and their omission in this study will be discussed later.

In this paper, we apply a river channel network [Total Runoff Integrating Pathways (TRIP); Oki and Sud 1998], which provides flow directions, for river runoff data interpolation. The dataset has been interpolated to 1° grid boxes based on TRIP (Fig. 1b). The aim of TRIP is to provide lateral water movement information over land following the paths of river channels. The TRIP map was used to prepare templates to convert the station data of river discharge into the areal data of mean runoff depth. In this study, the measured runoff data at a runoff station are divided by the corresponding basin area first to obtain the runoff depth in the basin. They are, then, uniformly assigned to the grid points within this river basin according to flow direction of the TRIP.

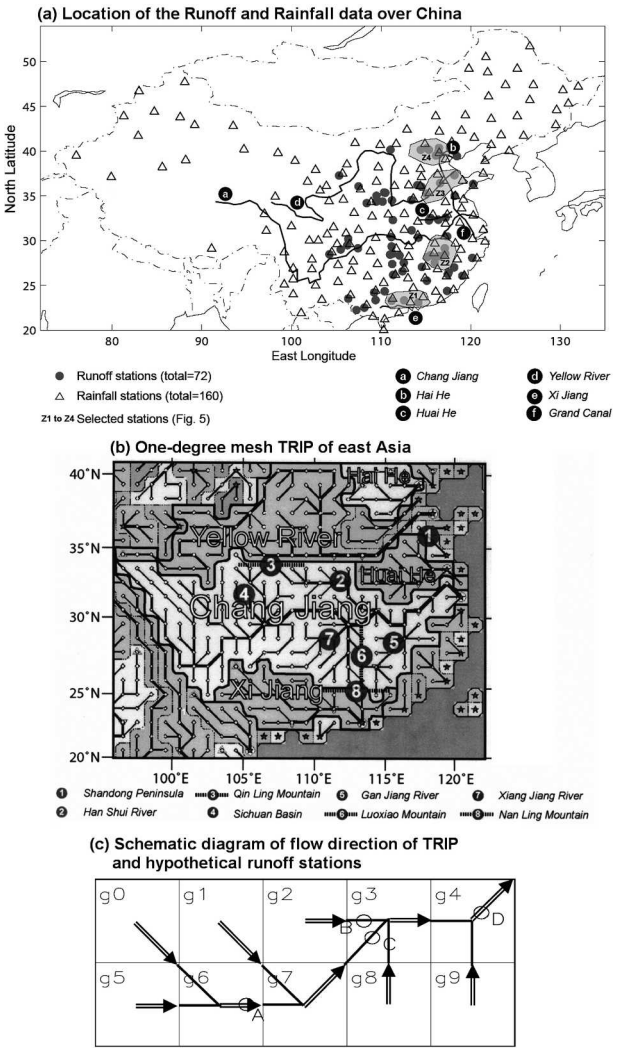

FIG. 1. (a) Location of the runoff and rainfall stations over China (circles: runoff stations; triangles: precipitation stations); and (b) extraction of the one° mesh TRIP of Asia (from Oki and Sud 1998). River mouths are plotted by "✶." The thick line corresponds to the river order of streams. (c) Schematic diagram of flow direction of TRIP and hypothetical runoff stations.

If there are multiple stations in a river, the runoff depth in the upper reach is calculated first. In subsequent calculations of runoff depth to the lower reach, the discharge that is measured in the upper reach is subtracted from the measurement of the lower-reach station to obtain the discharge between these two stations. The similar procedure is done for the basin area between these two stations to finally get the runoff depth in the lower reach. If a grid box lies among different river basins, then the averaged runoff depth is assigned to that box. While conducting interpolation, we have to compare the TRIP with published river maps because some stations appear to lie consecutively in a river or to be concentrated within one grid box in the TRIP map, but they actually represent different parallel branches of a river. Careful checking must be done before subtracting the station runoff values and assigning the runoff depth to grid points. Figure 1c is a schematic diagram showing the flow direction of TRIP and hypothetical runoff stations. Double-lined arrows indicate the flow directions. Based on the principles described earlier, measurements at station A determine the runoff depth at grid points g0, g5, and g6; measurements at station B determine the runoff depth at g2. The measurement differences between station D and stations B and C determine the runoff depth at g4, g8, and g9. The runoff depth at g3 is determined by measurements at B, C, and D.

In addition to the runoff data, we have also obtained monthly mean precipitation data from the Chinese Academy of Meteorological Sciences. A dataset with 160 stations from 1951 through 1999 is used for this study (Chen et al. 1998). The spatial coverage for the precipitation data is relatively dense and well distributed in the eastern part of China (Fig. 1a). This dataset has also been interpolated to 1° grid boxes using Grid Analysis and Display System (GrADS) software (Doty 1995). We focus only on the areas to the east of 105°E because of the runoff data coverage. This region is referred to as east China (EC), and our discussions are restricted within this region. Please note that these two datasets were measured and recorded by two independent organizations: one is a meteorological network and the other is a hydrological network. This work intends to explore their variability and covariability at the continental and seasonal-to-interannual scales.

3. Basic climatology

The annual mean precipitation and runoff from 1951 through 1983 are shown in Fig. 2. Figure 2a has been compared with some published Chinese annual precipitation maps with unspecified average time periods and numbers of stations used (e.g., Xu 1990; Derbyshire 1990). The patterns and magnitudes in Fig. 2a are more similar to those in Fig. 2c (Derbyshire 1990) and in Xu's (1990) map than those produced using datasets with coarse resolutions over the China region (e.g., Xie and Arkin 1997; Hulme 1992). East China rainfall is greatly influenced by the East Asian summer monsoon and is inversely related to distance from the sea. Figure 2a exhibits a clear south–north gradient as well as an east–west gradient, which is consistent with the monsoon migration. The 700-mm isohyet roughly follows the northern boundary of the Huai He River basin and Qin Ling Mountain (label 3 in Fig. 1b), and is a divide between the rice areas and the dry farming lands. To the north of the 500-mm isohyet, precipitation is scarce, resulting in mainly pastoral areas (Zhao 1986). The heaviest precipitation with more than 1600 mm annually occurs along coastal areas that are associated with hills and mountains.

In winter [December–January–February (DJF)], with the strong northerly monsoon, the climate is cold and dry resulting from the dominant Siberian cold system (Fig. 3a). Except to the south of the CJR, where precipitation stems mainly from the lifting of warm, moist southerly flows by cold bursts from the north, the monthly rainfall mean is less than 40 mm month^{-1} over most of the region. The rainy season in East Asia starts in April from south of the CJR and moves southward in May to south China with light precipitation. This is caused by the confluence of cold air from the north, the southwesterly flow from the subtropical high, and westerly flow from the subtropical region of South Asia, forming a typical subtropical rainbelt. The monsoon from the South China Sea reaches southeast China in late May. Figure 3b shows March–April–May (MAM) mean precipitation, when the areas to the south of the CJR receive about 40% of their total precipitation for the year. The monsoon moves northward during the summer [June–July–August (JJA), Fig. 3c], when the areas to the north of the YR receive more than 50% of their precipitation for the year, which is in dramatic contrast to the spring drought there. The precipitation to the south of the CJR consists of about 35% of the annual total. Because of the topographic effects that block the monsoon migration, the northwest part of EC has little precipitation, even during the summer. During the fall [September–October–November (SON)], the Sichuan basin (label 4 in Fig. 1b) receives more precipitation, which is about 25% of the annual total for that area (Fig. 3d). The ratios of seasonal precipitation to the annual precipitation for EC for DJF, MAM, JJA, and SON are 0.066, 0.256, 0.481, and 0.197, respectively.

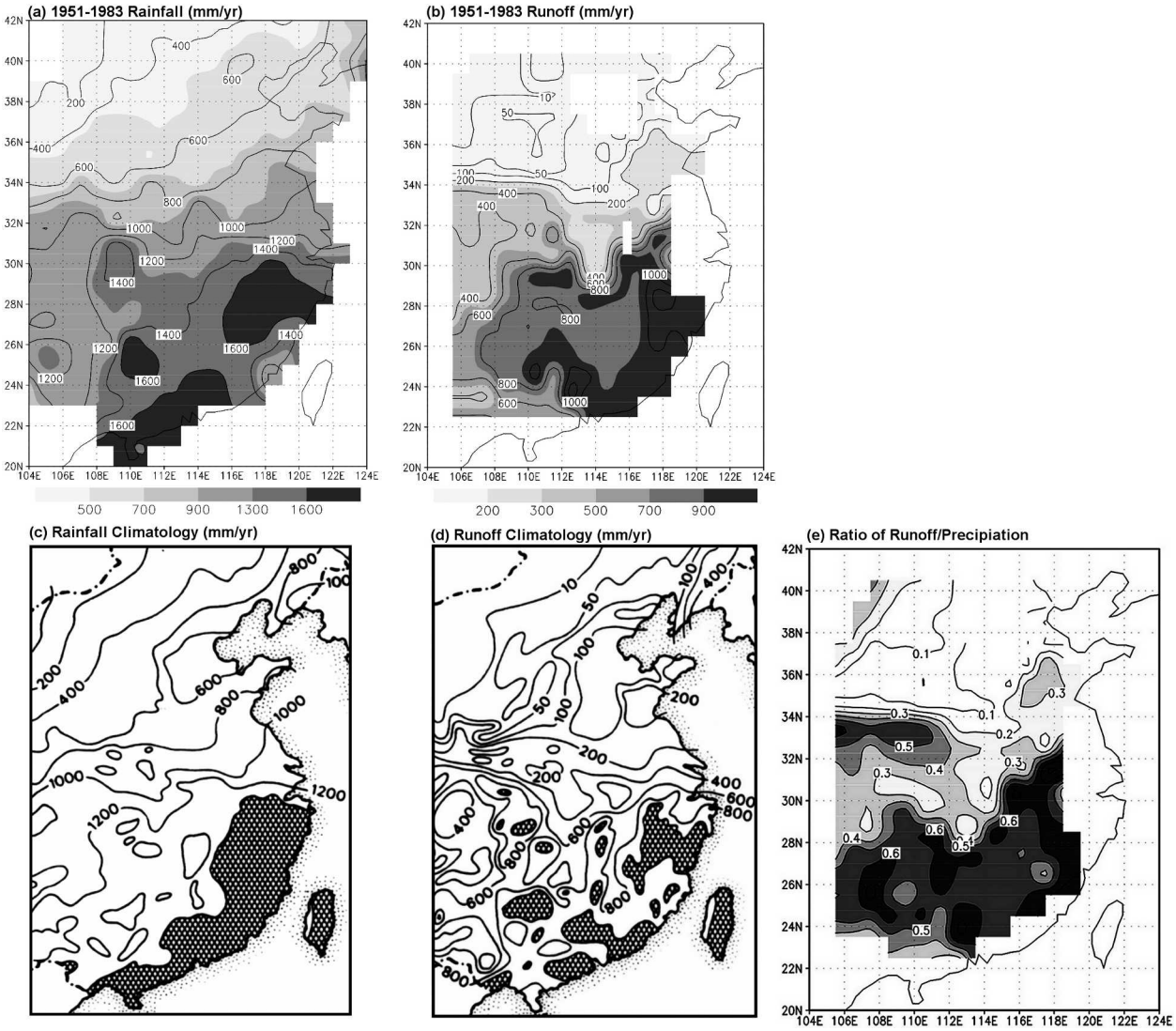

FIG. 2. (a) Mean annual precipitation and (b) runoff depth during the 1951–83 period from our study and (c) annual precipitation and (d) runoff depth from the *Hydrologic Atlas of the People's Republic of China* (Derbyshire 1990). Unit: mm yr^{-1}. The areas with more than 1600-mm precipitation and 1000-mm runoff depth are crosshatched in (c) and (d), respectively. (e) Annual ratio of runoff–precipitation during the 1951–83 period.

Clearly, the most abundant precipitation falls in the monsoon period of JJA.

These characteristics are also clearly exhibited in the runoff at the annual and monthly scales (Fig. 2b and Fig. 4). Please note that the spatial coverage of Fig. 2b around the periphery of the domain is different from Fig. 2a. This is an artifact of the spatial coverage of the steamflow gauges and the river flowchart. Figure 2d is the annual river runoff depth with unspecified average time period and number of stations from the *Hydrologic Atlas of the People's Republic of China* (Derbyshire 1990), which has been compared with other published high-resolution figures of runoff depth over China (Xu 1990; Technique Team of Preliminary Products of National Water Research 1981). The Technique Team of Preliminary Products of National Water Research (TTNWR) figure was based on data from 1956 through 1979, with an unspecified number of stations in China, and Xu (1990) did not provide detailed information. The maps that are based on these three datasets show similar major large-scale patterns. However, the regional detail and the magnitude are different, maybe as a result of the time period, number and spatial distribution of stations, and/or the interpolation methods used.

We analyze spatial patterns in Figs. 2b and 2d to

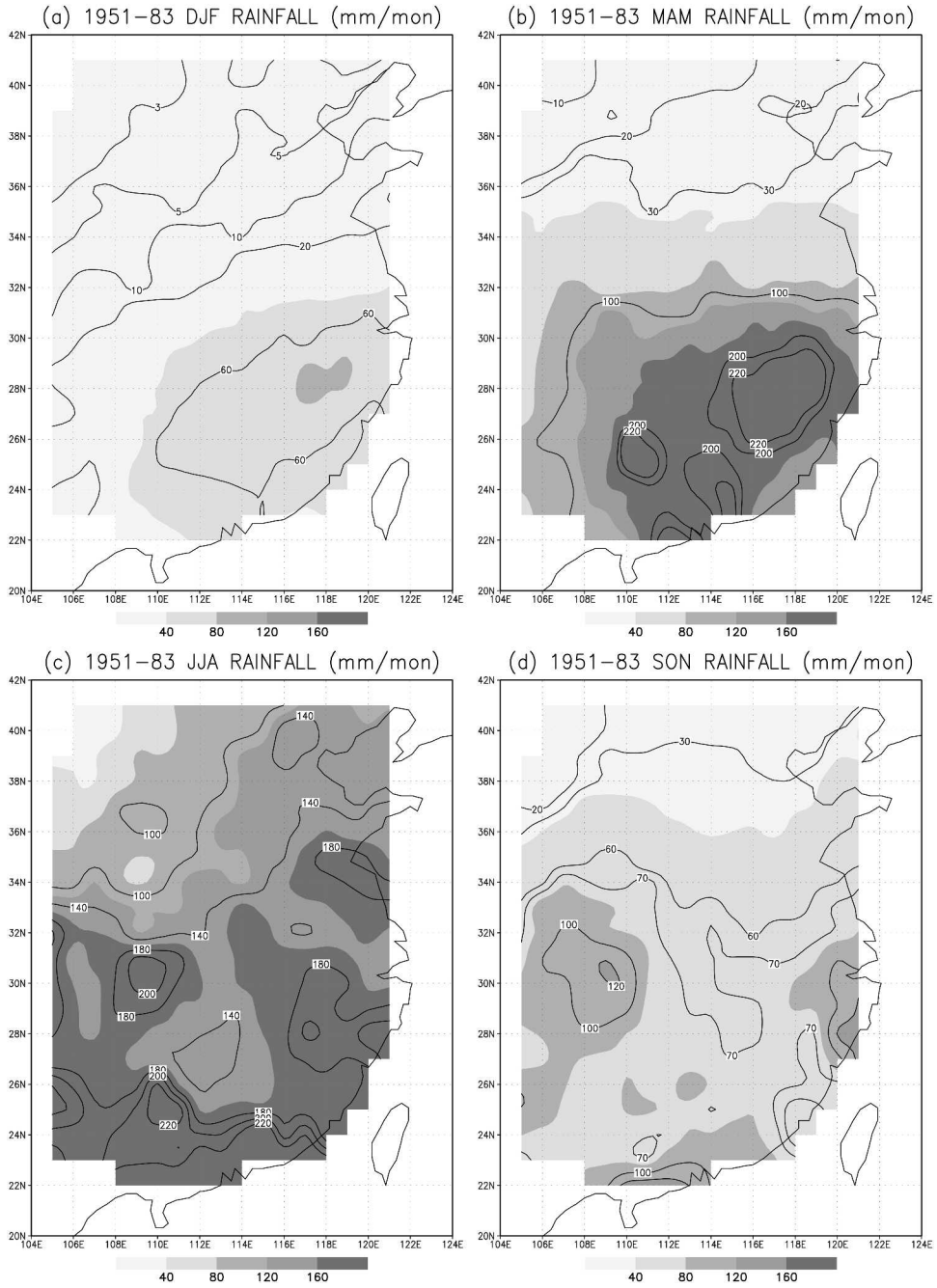

FIG. 3. Mean seasonal precipitation during the 1951–83 period (mm month^{-}): (a) DJF, (b) MAM, (c) JJA, and (d) SON.

understand the observed large-scale spatial variability of runoff, and to evaluate the gridded runoff data. The highest runoff is located to the south of CJR. The areas that are associated with high runoff (more than 900 mm year^{-1}) are located in the hills and mountains along the southeastern coast (around 27°N and 118°E), to the south of the Nan Ling Mountain (label 8 in Fig. 1b), and in the areas south of 30°N along 110°E (east of the Yun-Gui Plateau), consistent with Fig. 2d. However, a relative high along 114°E between 25° and 28°N is not produced in Fig. 2b. This area is the Luoxiao Mountain (label 6 in Fig. 1b), which separates two major southern tributaries of the CJR: the Xiang Jiang River and the Gan Jiang River (labels 7 and 5, respectively, in

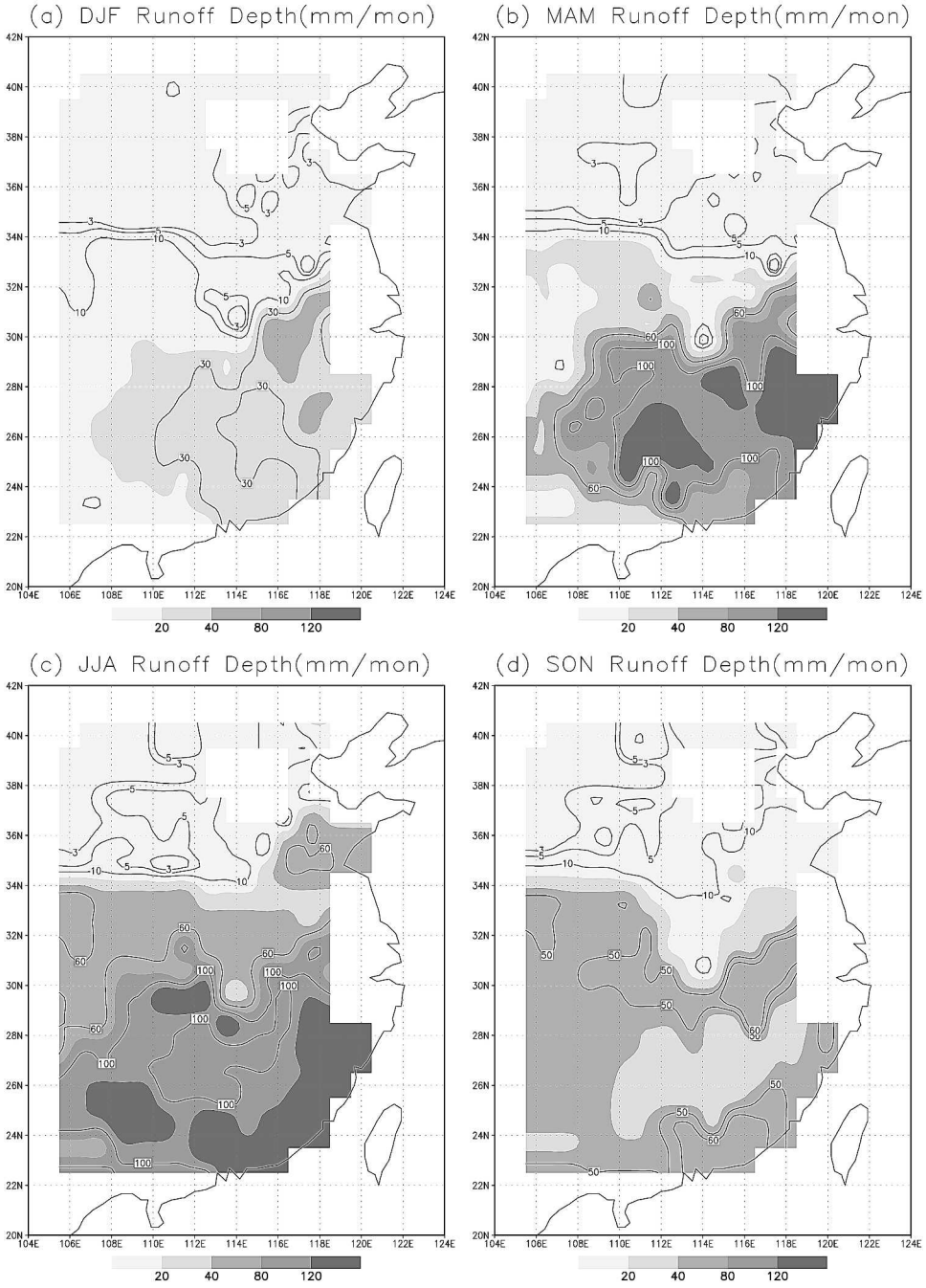

FIG. 4. Mean seasonal runoff depth during the 1951–83 period (mm month^{-1}): (a) DJF, (b) MAM, (c) JJA, and (d) SON.

Fig. 1b). We have insufficient stations over that area (see Fig. 1a) to highlight this regional pattern. Aside from this shortcoming, the spatial features in this high runoff area are reasonably captured.

The Sichuan basin in western China created a special spatial runoff feature. The Sichuan basin has low runoff but is surrounded by relatively high river runoff depth in Fig. 2d that is associated with high topography. Although this feature appears in Fig. 2b, the magnitude of high runoff in surrounding areas is about 200 mm yr^{-1} lower than in Fig. 2d. The presence of fewer stations in that area (Fig. 1a) may contribute to this discrepancy.

To the north of the CJR, the spatial variability of runoff is highlighted by several isobaths. The

400 mm yr^{-1} isobath generally follows the CJR and Qin Ling Mountain with a dip around 114°E and 31°N, which corresponds to the Han Shui River basin (label 2 in Fig. 1b), a northern tributary of the CJR. This feature is consistent with Fig. 2d and with Fig. 2a, which show a similar dip in spatial distribution of precipitation. The 200-mm isobath line is along 34°N in the western part of EC, which is also an important divide; there are subtropical broadleaf and evergreen forests to the south and a forest–steppe vegetation zone to the north. The 200 mm yr^{-1} isobath in Fig. 2d in east EC is close to the mouth of the CJR. According to Xu (1990) and the Technique Team of Preliminary Products of National Water Research (1981), it should be extended to the Shandong Peninsula (label 1 in Fig. 1b), as shown in Fig. 2b. The 50-mm isobaths in both Figs. 2b and 2d extend northeast to southwest over the area to the east of 112°E, with a semiarid steppe zone to the northwest. By and large, Fig. 2b produces major EC runoff features. The consistency between Figs. 2a and 2b, which come from two different sources, and between these and other published precipitation and runoff depth maps, indicate that our interpolation method is appropriate for this study.

Two rivers in China provide a distinct boundary for the runoff distribution: the runoff to the south of the CJR and the YR is substantially higher than that to the north of those rivers. The runoff is the product of the integrated action of many physical factors as well as human intervention. Comparing Figs. 2a and 2b, it is clear that precipitation is a very dominant factor for the runoff and they have very similar spatial distributions with many isobaths and isohyets corresponding to each other. But the runoff distribution is greatly modified by topography, human intervention, and climate/vegetation, as is evident in the Han He River basin, the Sichuan basin, and northern EC, as well as in many regional details in the runoff/rainfall ratio (Fig. 2e). On average, the runoff/rainfall ratio is more than 50% to the south of the CJR. The runoff is less than 35% of the rainfall total in the areas to the north of the CJR, with, for the most part, less than 15% to the north of the YR. These differences indicate that factors such as topography and other land conditions, which affect evaporation and infiltration, play important roles. For instance, in northern EC, vegetation plays a more important role for runoff through evaporation than in southern EC, where the actual evaporation is closer to potential evaporation as a result of the humid climate. Human intervention may also contribute to the lower runoff in northern EC. For example, although the area of the Hai He River basin covers only 0.6% of China, it contains 10% of the Chinese population. On average, during the 1980s, 67.7% of river runoff in this basin had been employed for different purposes. The average for China as a whole was only 15.3% (Institute of Chinese Water Resources and Electric Power 1989). We are not able to quantitatively assess human intervention on runoff in these areas. However, as discussed earlier, on an annual basis our runoff map in that area is consistent with the published maps.

The seasonal variations of the runoff distribution generally follow the seasonal changes in precipitation distribution (Figs. 3 and 4), especially in winter and spring, but still with quite different features at the regional scale. Based on analyzing the differences of the monthly precipitation and runoff between two consecutive months (not shown), the runoff, in general, has a direct response to the rainfall in the same month, in particular, from April to July. During the winter, the ratio of runoff to precipitation between 32° and 34°N and 105° and 110°E is larger than 1 (comparing Figs. 3a and 4a), which is likely the result of snowmelt. The mean surface temperature over that area is very close to freezing in that season (not shown).

During the summer, when the monsoon reaches northern EC, areas with high runoff depth still remain in the coastal region (Fig. 4c). Relatively low runoff in three major tributaries of the CJR—the Xiang Jiang River basin, the Gan Jiang River basin, and the Han Shui River basin—are evident, consistent with published annual runoff depth maps (i.e., Fig. 2d). In contrast to the surrounding mountains, the precipitation in basins and plains is usually less abundant and evapotranspiration is stronger, which leads to less runoff. Relatively high runoff (more than 50 mm $month^{-1}$) appears west of the Shandong Peninsula, corresponding to the northward monsoon migration. However, over other areas in northern China [mainly in the YR basin and the Hai He River basin (label b in Fig. 1a)], the increase of runoff is not substantial (Fig. 4c). As discussed earlier, high evaporation in this dry area could be expected after the dry spring. In northwestern EC, while the precipitation has a slight increase in May and June, the runoff decreases in the same area, reflecting a lag response resulting from evaporation and infiltration. Human intervention may also contribute to less runoff in northern EC as discussed earlier. The northern rivers tend to be highly regulated. Average storage capacity in the Hai He River basin is equivalent to about 90% of the average annual runoff, whereas the average for China as a whole is only 17% (World Bank 2001), which affects the amount of runoff and its timing.

At the end of the summer and during the fall, when the monsoon is retreating, the runoff still increases over several areas, which include some river networks of the

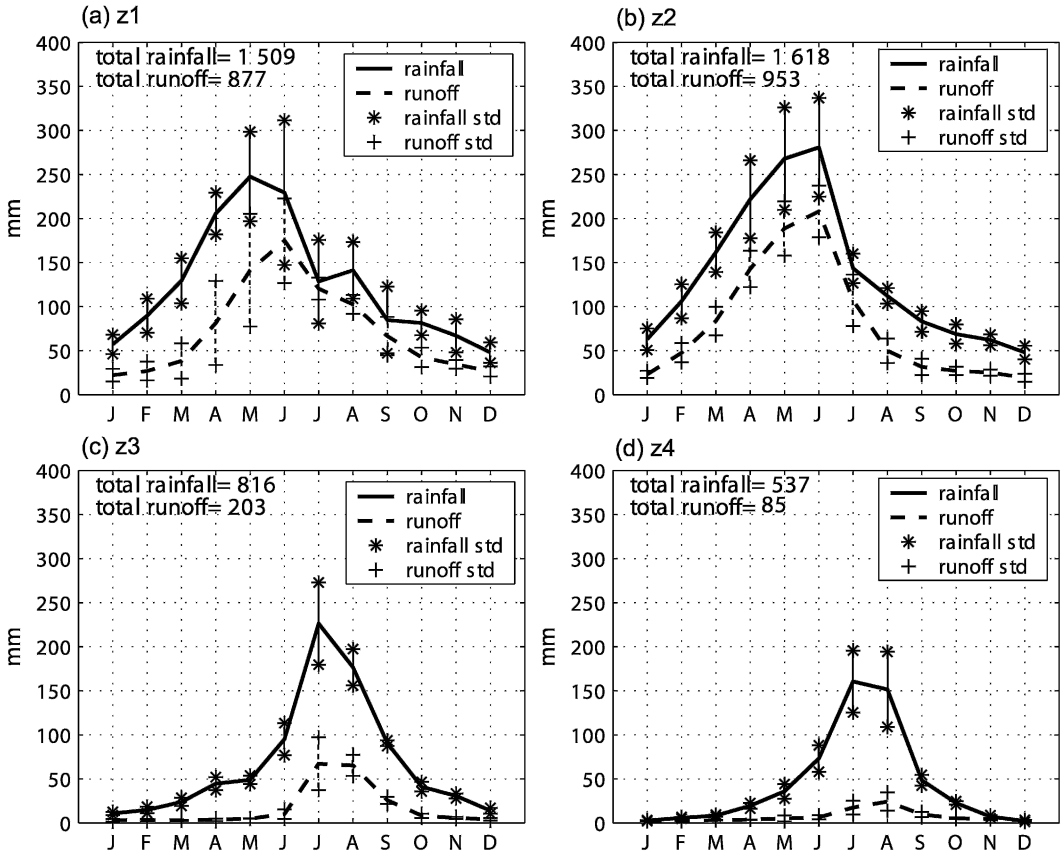

FIG. 5. Mean monthly time series of river runoff at four selected areas [(a) Z1, (b) Z2, (c) Z3, and (d) Z4, see Fig. 1a)] and the associated rainfall time series (mm month^{-1}). The standard deviations are also indicated.

CJR basin. A strong lag starts along 30°N between 105° and 119°E in August and moves downstream to between 110° and 115°E in September and between 110° and 118°E in October. The increase in fall precipitation over the Sichuan basin and surrounding mountainous regions (Fig. 3d) may also contribute to these runoff changes. The precipitation during that period in these regions is not that intense but is quite persistent. This lag still exists, even in December in an area near the mouth of the CJR. These lag responses are evident in Figs. 4d and 4a with a relatively high runoff along 30°N in eastern EC. The ratios of seasonal runoff depth over the annual runoff depth for EC for DJF, MAM, JJA, and SON are 0.09, 0.29, 0.42, and 0.20, respectively.

The seasonal variations of monthly mean river runoff and precipitation for four selected subriver basins (Fig. 1a) from the south to the north of EC are shown in Fig. 5. Some statistics are listed in Table 1. The shaded areas in Fig. 1a indicate the runoff and precipitation stations that we select. They belong to the Xi Jiang River (XJR)

TABLE 1. Some statistics for four subbasins (mm month^{-1}).

Subbasin	Maximum runoff (month)	Maximum precipitation (month)	Annual precipitation	Annual runoff/ precipitation	Correlation coefficient between runoff and rain
Z1*	175 (Jun)	248 (May)	1509	57%	0.75
Z2**	208 (Jun)	281 (Jun)	1618	52%	0.90
Z3	67 (Jul), 65 (Aug)	226 (Jul)	816	25%	0.76
Z4	24 (Aug)	160 (Jul)	537	16%	0.73

* Area Z1 has second precipitation peak in Aug (148 mm month^{-1}).
** Area Z2 has second high in May: 189 mm month^{-1} for runoff and 268 mm^{-1} for precipitation.

basin (Z1 in Fig. 1a), the Gan Jiang River basin (Z2), the YR basin (Z3), and the Hai He River basin (Z4). In area Z1, the maximum runoff and rainfall have a 1-month lag. The runoff peak occurs in June, corresponding to the monsoon onset in May and heavy rainfall in June (Fig. 5a). The time series of precipitation is characterized by two peaks. The main one is in May, and the second one (relatively weak) is in August while the monsoon retreats. For the associated runoff time series, no clear second peak appears in August. But the runoff persists from October through March. In the case of area Z2, both precipitation and the runoff reach maximums in June (Fig. 5b). But runoff and precipitation in May are also substantially high. This is because the subtropical rainband starts from the south of the CJR in April and moves southward. In mid-May, after monsoon onset, the East Asian monsoon moves northward from the southern coastal area of EC. Wet soil moisture conditions in the Z2 area contribute to higher runoff in May. This area also has persistent fall and winter runoff, as is evident in Figs. 4a and 5b. For the two northern areas, the runoff peaks occur in July and August in area Z3 (Fig. 5c) and in August in area Z4 after the monsoon moves into these areas. The runoff peak in August is 1 month later than the July rainfall maximum. The runoffs in fall, winter, and spring are very low in Z3 and Z4. The precipitation peak in Z3 is not much lower than in Z1 and Z2, but the total is lower and precipitation is mainly concentrated in the summer. The annual precipitations for Z3 and Z4 are about or less than half of the precipitation in Z1 and Z2. The dry surface condition in spring, high soil infiltration, and high summer surface evaporation, as well as human intervention, may contribute to the lower runoff in addition to precipitation. The different runoff/precipitation ratios in different areas (Table 1) are an indication of the effects of climate and surface soil moisture and vegetation conditions, and probably human intervention.

4. Spatial and temporal summer precipitation and runoff patterns

Because 42% of the total runoff and 48% of the total precipitation in EC occur in JJA, we will mainly focus on JJA in this and the next sections. The summer rainfall in EC is characterized by lower relative variability with the coefficients of variation (CV, standard deviation divided by mean) between 0.25 (southern part) and 0.4 (northern part). On the other hand, with a lower mean value and higher standard deviation, the summer runoff has a higher CV than precipitation (Fig. 6). In particular, northern EC, with less precipitation, has higher relative variability in runoff than southern EC. To the south of the CJR, the CVs in runoff range from 0.3 (over southwest EC) to 0.4 (over the middle DJR reaches), while to the north of the CJR, CVs range from 0.6 to 0.9, which are consistent with the Institute of Chinese Water Resource and Electric Power's (1989) estimations. The high CV center in northern EC, located over the southwest of the Shandong Peninsula, is also consistent with TTNWR's report (Technique Team of Preliminary Products of National Water Research 1981). The CV for the runoff over the Shichuan basin is about 0.2, which is lower than the published value (about 0.4) for that area (Technique Team of Preliminary Products of National Water Research 1981), which is likely the result of a lack of stations over that area (Fig. 1a).

The dominant spatial and interannual temporal patterns of both JJA precipitation and runoff datasets and their correlations are studied with EOF analyses (North et al. 1982; North 1984; Storch and Zwiers 1999). The EOF method allows for the individual extraction of the main patterns of each variable. The EOFs are orthogonal spatial patterns that can be thought of as empirically derived basic functions. The low-order EOFs can sometimes be interpreted as natural modes of variation of the observed system. The time coefficients that are obtained by projecting the observed field onto the EOFs, called principal components (PCs), are uncorrelated and represent the temporal variability of the field. For the precipitation and runoff anomaly fields, the climatological seasonal cycles, defined by the average annual cycle for the data period, have been removed prior to the application of the EOF analyses. In the temporal domain, each PC from EOF analyses is scaled by its standard deviation. The spatial pattern is then multiplied by its corresponding PC's standard deviation. In WLX99's study, the characteristics of Chinese precipitation have been comprehensively discussed. We will only briefly present some major features of the Chinese precipitation for the time period that was investigated in this study for purposes of comparison with the runoff.

The spatial patterns and their corresponding PCs for the first three EOF modes of the summer precipitation are shown in Fig. 7. The results for the first two EOFs in Fig. 7 are similar to two EOFs shown by WLX99, but with higher variances for each EOF. $EOF1_p$ explains 22.2% of the total variance of summer rainfall. We use the suffixes p and r to denote the precipitation and runoff EOFs, respectively, in this paper. Unless otherwise specified, the description of spatial patterns in this paper is for a positive corresponding PC. $EOF1_p$ is characterized by a sandwich-type pattern—a negative–

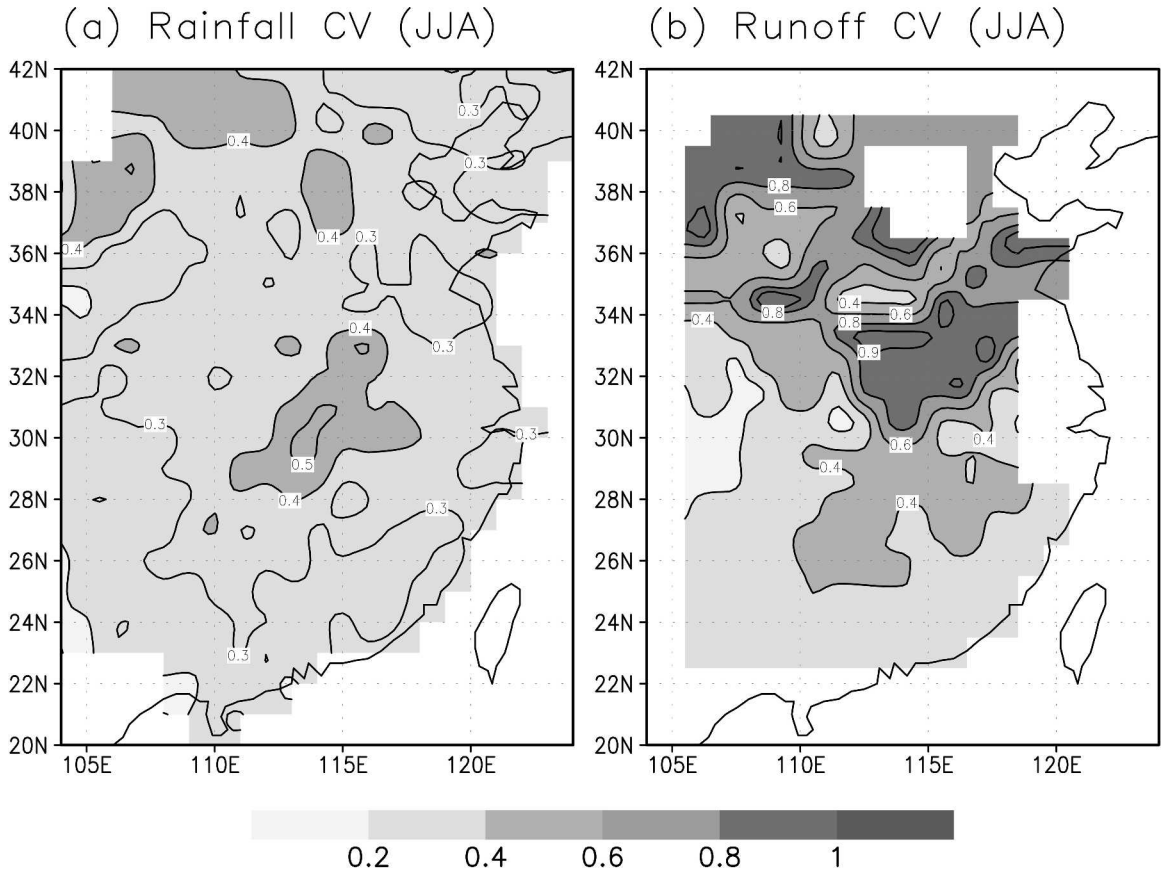

FIG. 6. (a) JJA rainfall and (b) runoff CV during the 1951–83 period.

positive–negative (NPN) pattern. The variation of summer precipitation in central EC, mainly the CJR basin, is opposite to the variability in the areas to its south (south of Nan Ling Mountain) and most parts to its north (north of YR). In $EOF1_p$, there is a maximum in the middle reaches of the CJR—a major flooding area in a number of extremely large flood events (e.g., the 1954 flood). PC1 is negative most of the time during 1959–78. WLX99 indicates that a prominent characteristic of $PC1_p$ is the sudden climate region shift after 1978, which is not clear in Fig. 7b because of the shorter period length in this dataset.

$EOF2_p$ explains 12.4% of the total summer precipitation variance. It shows a positive–negative–positive (PNP) pattern with the CJR as the boundary dividing the major positive pattern and the negative pattern (Fig. 7c). The maximum positive anomalies are located in the EC mountain and hill areas, and the major negative anomalies are in the Huai He River basin (label c in Fig. 1a), the Han Shui River basin, and the Shichuan basin. $EOF3_p$ explains 9.2% of the total variance and represents the southeast–northwest gradient, that is, coastal/inland opposition. Because the sampling error for $EOF3_p$'s eigenvalue is 2.31 [based on North et al.'s (1982) criteria], which is larger than the spacing between $EOF3_p$'s and $EOF4_p$'s eigenvalue, it indicates that $EOF3_p$ has large uncertainty. We will not discuss it further, but we believe that this southeast–northwest gradient is an important physical characteristic of Chinese rainfall and, therefore, we retain this figure for further validation.

Using the runoff data from 1951 to 1983, three summer runoff EOFs and PCs are shown in Fig. 8. $EOF1_r$ explains 32.1% of total summer runoff in EC. The positive anomalies cover the XJR, the Huai He River, and the CJR, with the maximum positive anomalies being located between the CJR and Nan Ling Mountain, where two major southern tributaries—the Gan Jiang River basin and Xiang Jiang River basin—are located. These areas represent the major standard deviations in this runoff dataset (not shown) and are also generally consistent with the spatial distribution of positive maximums in $EOF2_p$. The negative anomalies cover the Shandong Peninsula and the Qin Ling Mountain area. The standard deviation, especially the CV (Fig. 6b), is considerably higher in the Shandong Peninsula. The

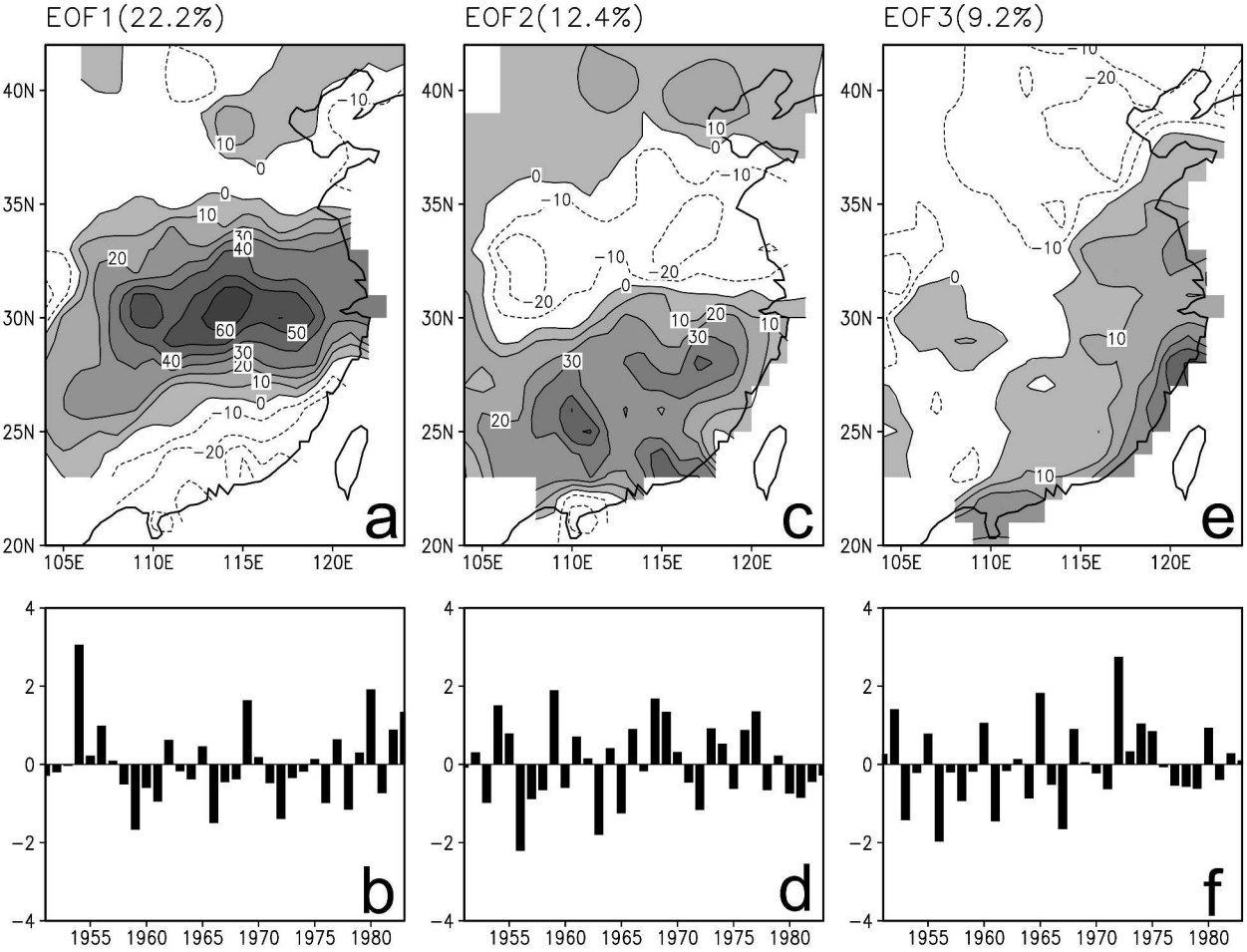

FIG. 7. Summer (JJA) rainfall (top) EOF spatial pattern and (bottom) PC time series during the 1951–99 period (mm month^{-1}): (a), (b) EOF1, (c), (d) EOF2, and (e), (f) EOF3.

negative anomaly areas are generally in agreement with the negative areas in EOF2$_p$. The temporal patterns of PC1$_r$ (Fig. 8b) are also similar to PC2$_p$, with the correlation coefficient between PC1$_r$ and PC2$_p$ being 0.77.

A wavelet analysis (Weng and Lau 1994; Torrence and Compo 1998) has been conducted to more clearly show the temporal variability. Figure 9a shows the real part of the Morlet wavelet coefficients of PC1$_r$ for time scales between 2 and 16 yr during the 33 yr. The signals with large variability are mainly on the shorter, interannual scales. A 6-yr, as well as a 16-yr, cycle are quite stable, both of which are generally synchronized with their counterpart in PC2$_p$ (Fig. 2b in WLX99) during the 33-yr period.

EOF2$_r$ explains 20.3% of the variance of total summer runoff in EC and represents opposite anomaly patterns in the southern coast area and the area to the north of Nan Ling Mountain (Fig. 8c). The maximum positive anomaly is over the XJR basin, which also represents the major standard deviation in the runoff dataset. The areas with maximum negative anomalies are located between the CJR and the YR, that is, over the Han Shui River basin. EOF2$_r$ has similar spatial and temporal variations compared to EOF1$_P$ (Fig. 7a). The temporal correlation between PC2$_r$ and PC1$_p$ is 0.71. But, as in EOF1$_r$, the spatial patterns in EOF2$_r$ are also very closely associated/modified with/by the river basins. Similar to EOF1$_r$, the signals with large variability are on the shorter interannual or interdecadal scales (Fig. 9b). A 10-yr cycle was strong in the 1950s, but gradually gave way to the component with shorter time scales (some 5-yr cycles), until a 13-yr cycle became dominant in the 1970s. These two cycles and their variations during these decades are quite consistent with the wavelet analysis on the variations in EOF1$_p$ (Fig. 2a in WLX99). The high correlations between precipitation and runoff EOFs are also consistent with the four regions that we reported in Table 1.

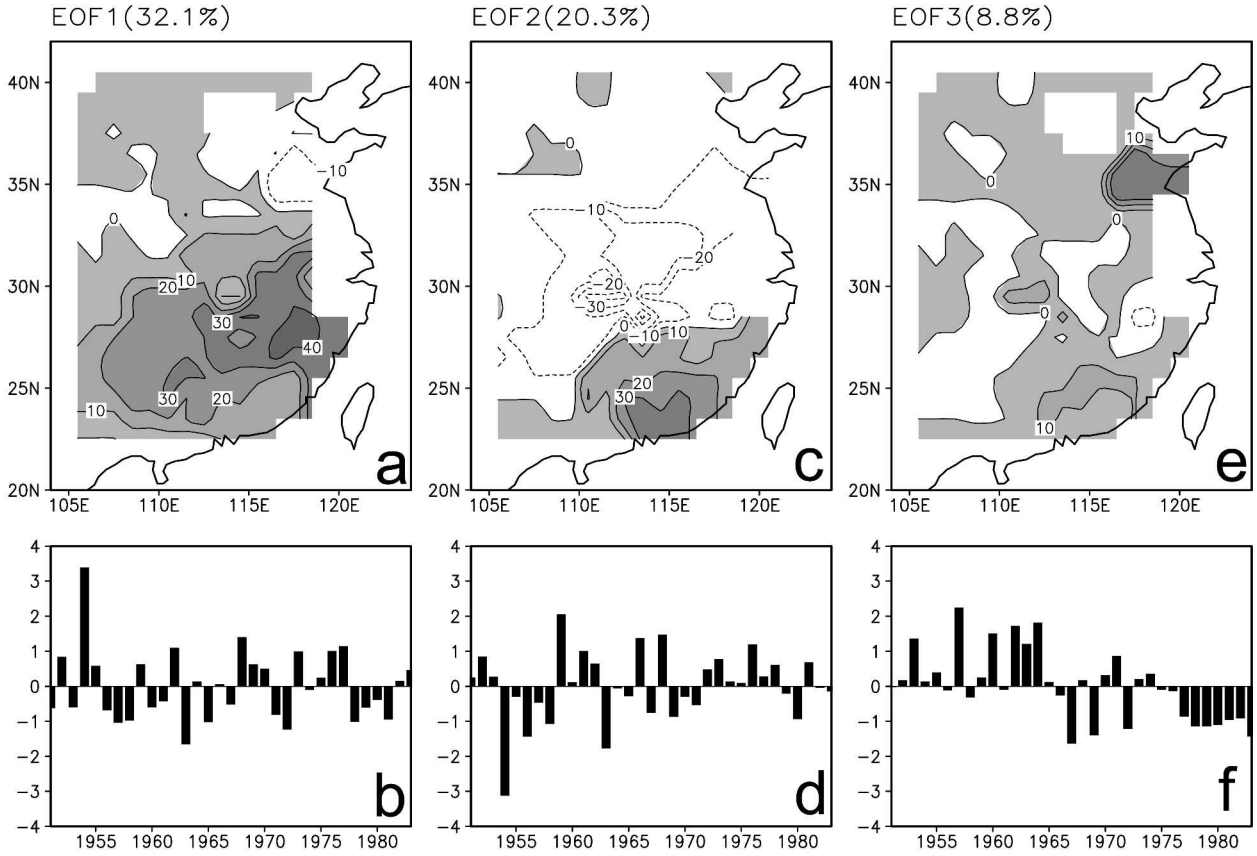

FIG. 8. As in Fig. 7 but for runoff during the 1951–83 period.

EOF3$_r$ explains 8.7% of the total variance; it represents a PNP anomaly pattern in a south–north direction and also gradients in a west–east direction. PC3$_r$ has a clear trend, which produces dry conditions in northern EC and the southern coast area and wet conditions along the CJR area after 1968. The spacing between EOF3$_r$'s and EOF4$_r$'s eigenvalue is smaller than the sampling error for EOF3$_r$'s eigenvalue. For the same reason as EOF3$_p$ we also report it in this paper.

The analyses from these modes show temporal variability at interannual and longer time scales. Different modes have different signs over different subareas and time periods. The climate anomaly patterns are determined by the dominant mode and interactions between the modes. This kind of complexity produces complex climate anomaly patterns.

5. Correlations between summer runoff, precipitation, and SST

EOF analyses in the last section indicate that runoff PCs consist of cycles close to the typical El Niño time scales (averaged as 3–6 yr). Numerous studies have been conducted to investigate the relationship between SST and rainfall variability over China (e.g., Wang and Li 1990; Simmonds et al. 1996). It has been found that although there is no consistent relationship between El Niño and rainfall over China as a whole (Ropelewski and Halpert 1987), some subdivisions in China present distinguishable modes of precipitation that were related to SST and El Niño (e.g., WLX99; Lau and Weng 2001). No effort has been made to investigate the relationship between continental-scale EC runoff and SST. We used the monthly mean SST data from the United Kingdom Hadley Center (Parker et al. 1999) with 1° horizontal resolution for this study.

The multivariate ENSO index (MEI), developed by Wolter and Timlin (1993, 1998), is applied in this study to evaluate its relationship with runoff. The MEI is calculated from an analysis of sea surface and air temperatures, and other meteorological variables recorded over the tropical Pacific region. The index is computed every month using information recorded during the preceding 2 months. The MEI time series are computed at bimonthly time scales (and are available online at http://www.cdc.noaa.gov/ENSO). The time series of ev-

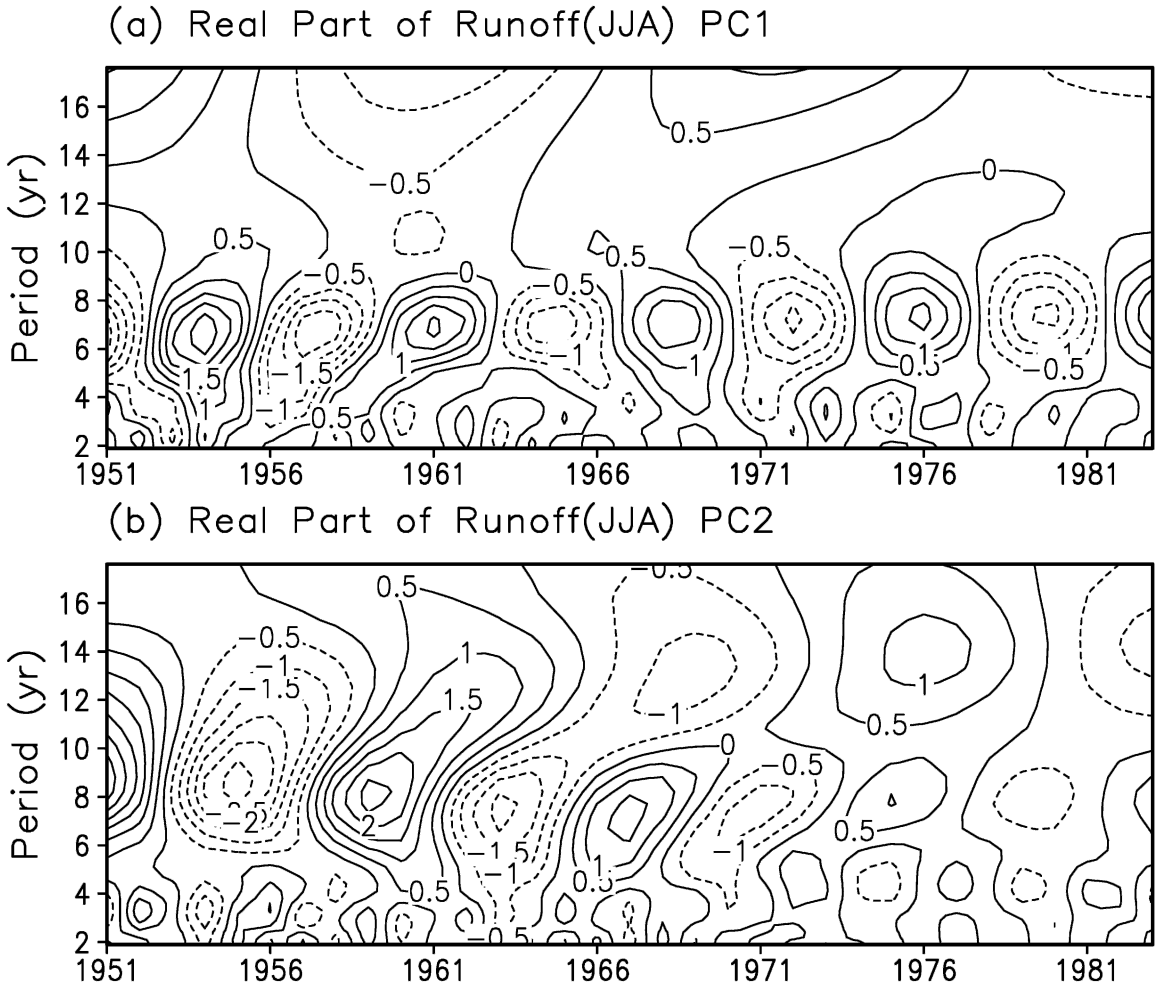

FIG. 9. Wavelet coefficients for (a) PC1 and (b) PC2 of the JJA runoff EOF modes.

ery month's MEI from 1950 to 1983 is used to calculate the correlation coefficients with runoff PCs.

The correlation coefficients between 12 MEIs and three summer runoff PCs and three summer precipitation PCs are shown in Fig. 10, in which the temporal correlation coefficients ±0.29 and ±0.34 have 90% and 95% statistic significance level, respectively, and are indicated by dashed lines. Figure 10 shows that most months' MEIs with $PC1_r$ and $PC3_r$ have correlations with more than 90% statistic significance. In particular, November/December, June/July, and July/August MEIs have more than 95% significant correlations with $PC1_r$; and December/January, March/April, April/May, May/June, and June/July MEIs have more than 95% significant negative correlations with $PC3_r$. This indicates that winter and summer SSTs may have more effect on summer runoff. The correlations for $PC2_r$ are quite low, consistent with $PC2_r$'s temporal scales that are revealed in wavelet analysis (Fig. 9b). Similar computation with precipitation fails to find correlations with more than 90% significance level (Fig. 10).

To further delineate these relationships, the runoff and precipitation PCs of EOF1 and EOF2 are regressed to SST at every grid point. Figure 11 shows each mode's regression map. The contour interval is 0.1°C. The areas with more than 90% statistic significance level, which largely appear in Figs. 11b and 11c, are shaded. Because of the high correlation between $EOF1_r$ and $EOF2_p$, it is not surprising to see some similarity between Figs. 11b and 11c. Both figures show the warmest anomalies in the eastern tropical Pacific, mainly in the Niño-3 region. However, the areas that are associated with 90% statistic significance level in Fig. 11c are much larger than in Fig. 11b, consistent with our MEI analysis. Furthermore, SSTs in some midlatitude areas also show a statistically significant relationship with EOFs (Figs. 11a–d), especially over some parts of the western Pacific, that is, to the east of the Philippines, Taiwan,

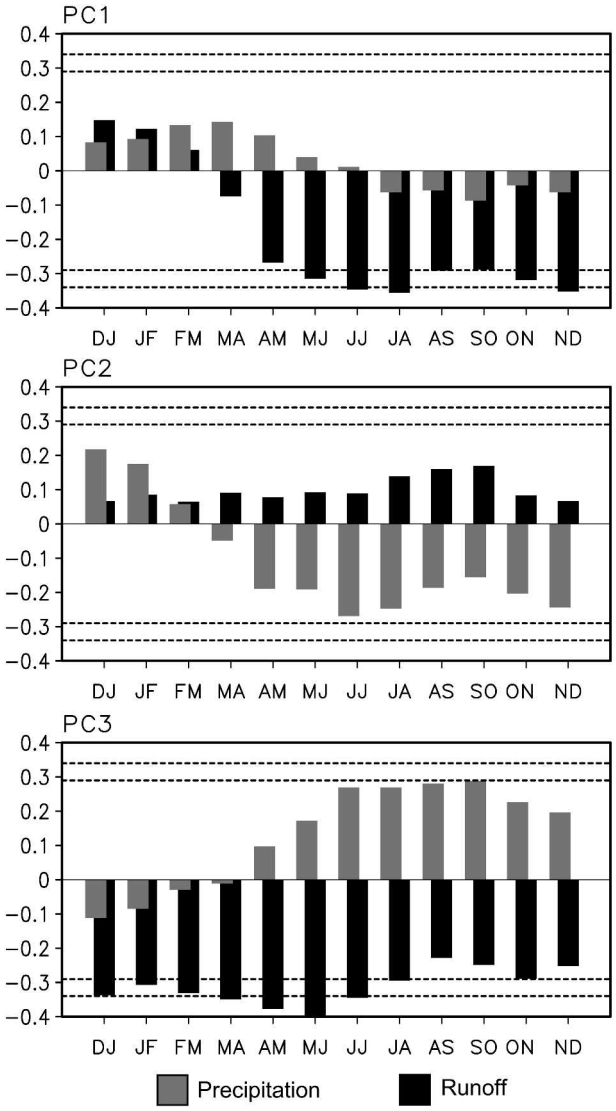

FIG. 10. Correlation coefficients between MEI and EOF PCs of summer (JJA) runoff depth and precipitation. Gray bar: precipitation; black bar: runoff: (top) PC1, (middle) PC2, and (bottom) PC3.

and Japan. In addition, Fig. 11d shows that the results over part of the Indian Ocean also have more than a 90% significance level. These results indicate that SST variations underlie these EOF patterns. EOF1 of runoff and EOF2 of rainfall are clearly related to El Niño, while EOF2 of runoff and EOF1 of rainfall are related to a dipole SST anomaly pattern over the northwestern Pacific. Studies (e.g., Lau et al. 2000) have shown the importance of this dipole pattern in governing rainfall variability over East Asia.

To further study the decadal relationship between the JJA SST, JJA precipitation, and JJA runoff, singular value decomposition (SVD) analysis was conducted. SVD allows focus on the common patterns between two variables (Wallace et al. 1992). SST, precipitation, and runoff are filtered using a recursive low-pass filter (Kaylor 1977), which is one of the infinite impulse response filters. It filters oscillations with less than 8-yr cycles in this study. The data anomalies have been normalized by their standard deviations first, and SVD analyses on SST/precipitation and SST/runoff covariability are conducted. We focus on the variability rather than absolute amounts in this section. Figures 12 and 13 show the first two SVD modes for precipitation and runoff, respectively. For comparison with runoff and for validation of the SVD calculation, we first briefly present precipitation SVD results. We use the suffixe *s* to denote the SST anomaly fields.

The first SVD mode of precipitation and SST explains 40.2% of the squared covariance between SST and precipitation. The spatial pattern (Fig. 12a) suggests an El Niño-like structure, with warm water in the tropical eastern Pacific, part of the western Pacific (to the east of Taiwan and the Philippines), and the Indian Ocean. There are two extensive and strong cold pools in the extratropical Pacific in both hemispheres. This pattern seems to be more connected with the ENSO-like interdecadal SST signal (Zhang et al. 1997). It may also be partially associated with the "linear trend signal" based on 50 yr of SST (Lau and Weng 1999) and the long-term signal that is associated with increased CO_2 warming based on coupled model experiments (Knutson and Manabe 1995, 1998). The correlations are very high for both positive and negative anomalies, with many areas having correlation coefficients that are higher than 60%, indicating more than a 99% statistic significance level. $PC1_s$ and $PC1_p$ (Fig. 12c) are also highly correlated (90% correlation), and exhibit pronounced interdecadal decadal variations with a warming trend after 1976. $SVD1_p$ is characterized by a NPN pattern. The variation of summer runoff in central EC, along the CJR basin, is opposite to the variability in the areas to its south and to its north, especially the Shandong Peninsula. $PC1_p$ indicates that there is a dry trend in northern and southern EC and a wet trend in central EC after the middle of the 1970s. This suggests that the NPN rainfall pattern has a strong decadal to long-term signal in addition to an interannual variability signal (as shown in Fig. 7).

The fraction of the squared covariance that is explained by $SVD2_p$ of precipitation and SST is 18.2%, with the correlation between $PC2_s$ and $PC2_p$ being 90%. The SST distribution ($SVD2_s$, Fig. 12d) features a wavelike structure linking the Tropics, subtropics, and the extratropics in the eastern part of the North Pacific

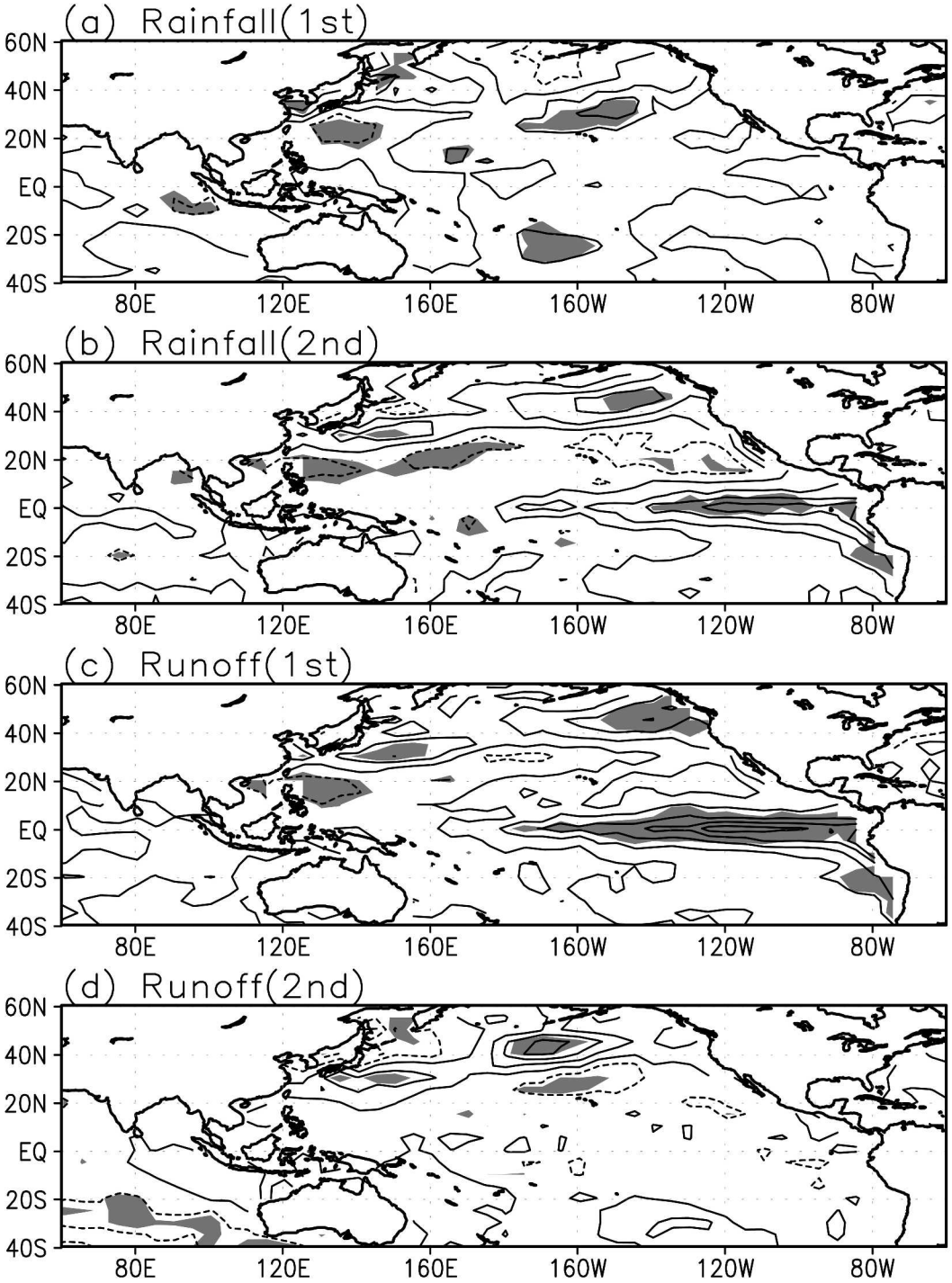

FIG. 11. Regression of precipitation and runoff PCs onto SST. Unit: °C; interval: 0.1. Based on (a) $EOF1_p$, (b) $EOF2_p$, (c) $EOF1_r$, and (d) $EOF1_r$.

basin. This wave train consists of relatively warm water in the Tropics and extratropics, and cold water in the subtropics off of the southwest coast of North America. But there are no organized anomaly patterns in the western Pacific and the Indian Ocean. The spatial pattern in $SVD2_p$ shows a southeast–northwest gradient. $PC2_s$ and $PC2_p$ exhibit one cycle in the 33-yr period. After the 1970s, this cycle produces negative anomalies

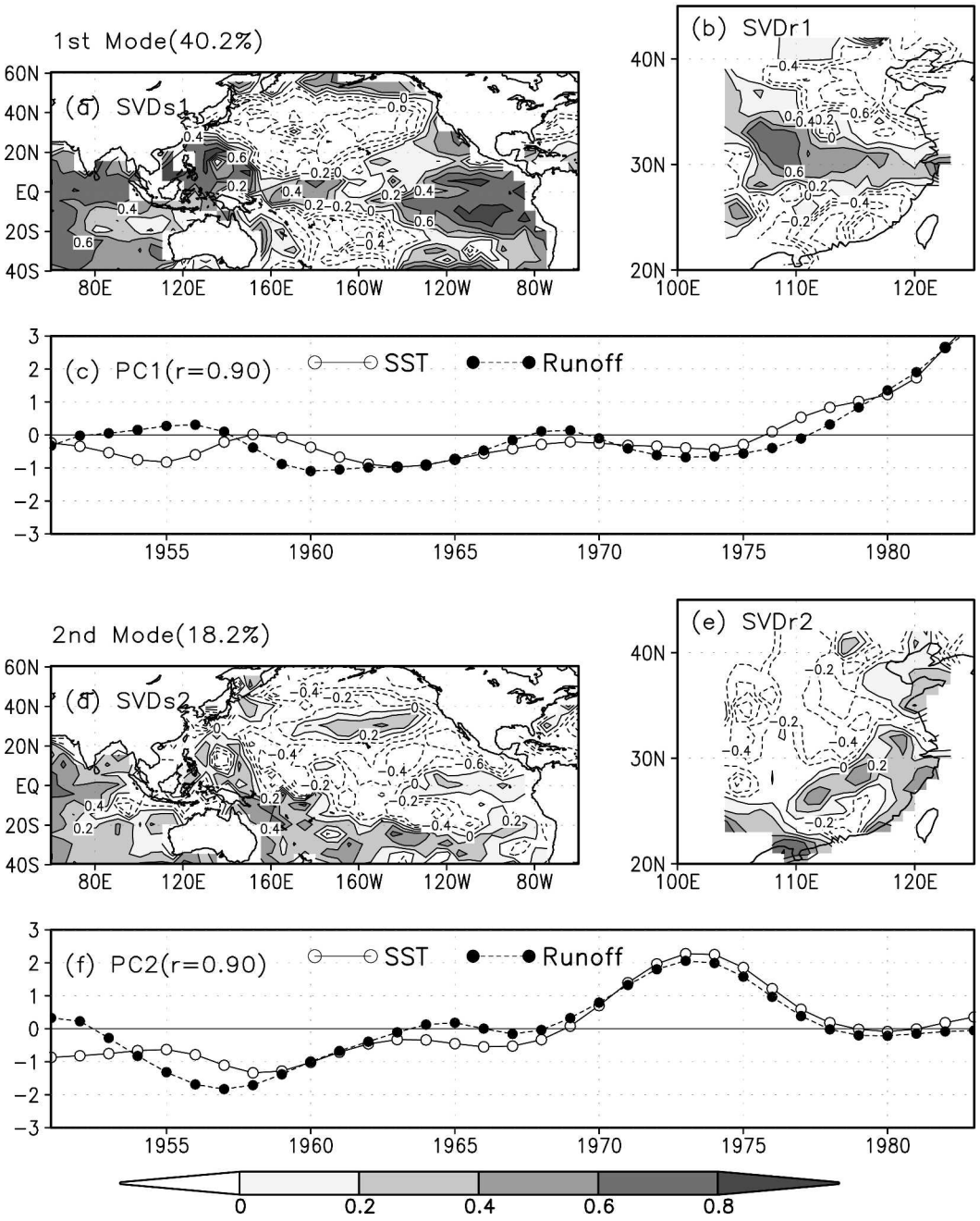

FIG. 12. Summer (JJA) SST and precipitation SVD spatial pattern and PC time series during the 1951–83 period. (top) first mode: (a) SVDs1, (b) SVDr1, and (c) PC1. (bottom) second mode: (a) SVDs2, (b) SVDr2, and (c) PC2.

over most parts of northern EC and positive anomalies in many areas over southern EC. SVD2$_p$ seems to be associated with an interdecadal signal of SST/rainfall, probably capturing part of the interdecadal signal left over from SVD1. It is believed that the actual precipitation variance that is associated with this mode may be very small. Hence, the long-term signal in SST/precipitation may be largely contained in SVD1.

The first SVD mode of SST and runoff explains 50.3% of the squared covariance between SST and runoff. The spatial pattern (Fig. 13a) shows warm water in the Indian Ocean and the eastern Pacific near the central and southern American coast. SVD1$_s$ is also a long-term trend signal that is mixed with an ENSO-like interdecadal signal. There are two cold pools in the extratropical Pacific in both hemispheres. But, the cool

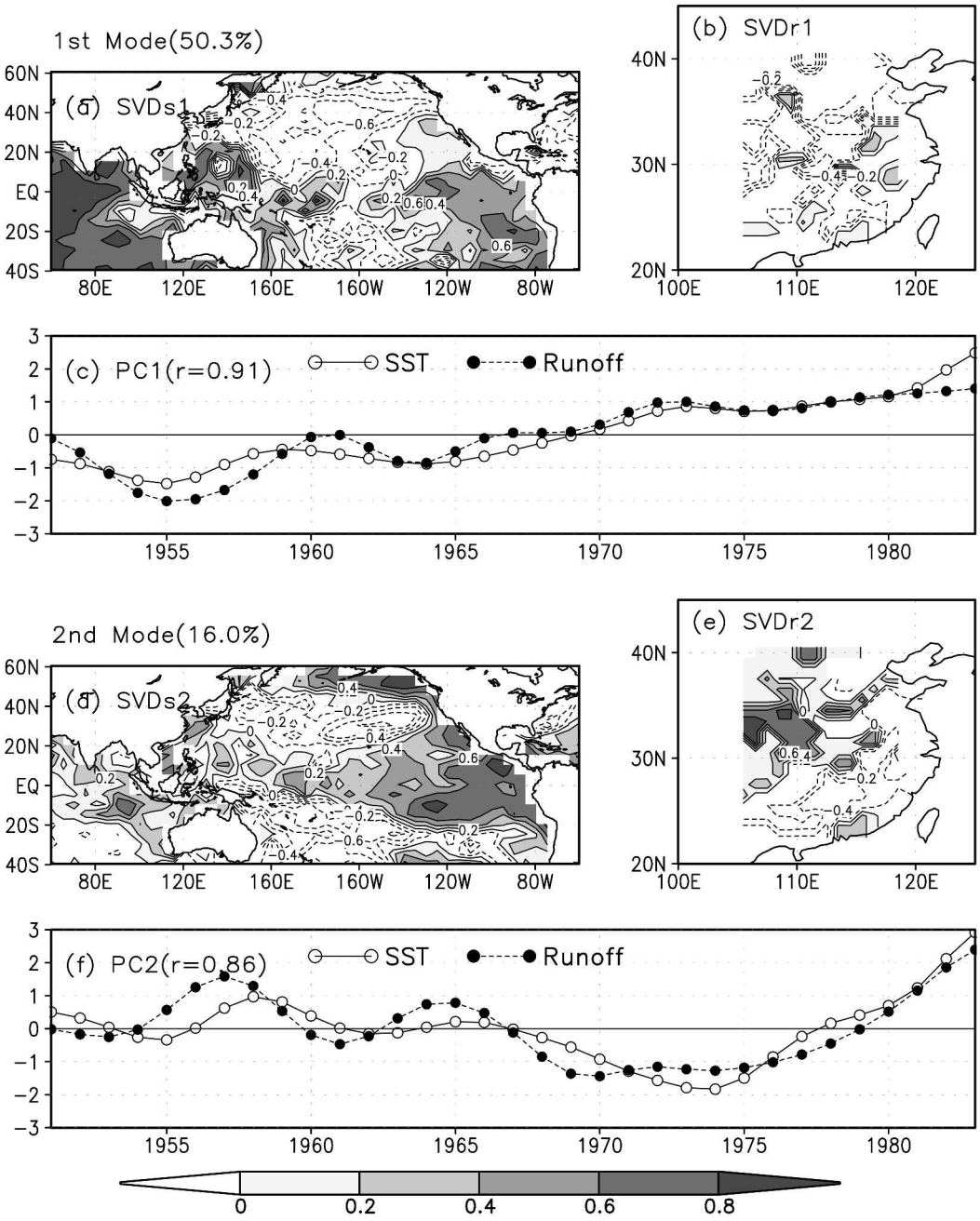

FIG. 13. As in Fig. 12 but for runoff.

SST anomaly signals are not as strong as in precipitation/SST SVD1$_s$, especially the anomalies in the southern Pacific. PC1$_s$ and PC1$_r$ (Fig. 13c) are very highly correlated (91% correlation) and exhibit a pronounced warming trend since 1955, which is noted in previous precipitation studies (Lau and Weng 2001), that is imposed to interdecadal variations. SVD1$_r$ shows a more homogeneous pattern over EC with a few opposite spots, including some areas along the XJR, the Huai He River, and the lower reach of the CJR (Fig. 13b). PC1$_r$ indicates that there is a dry trend in the river runoff over EC since 1955 corresponding to climate changes (Fig. 13c). The largest negative PC1$_r$ appears in the temporal series 1 yr after the major flood year, 1954. Because SVD1$_r$ has larger loading in northern EC after normalization of runoff anomalies, the results from SVD1$_r$ suggest that the trend signal is mostly in northern China. The dryness is highly related to the SSTs in

the eastern Pacific and the Indian Ocean. It is interesting to note that runoff variability seems to have more clear signatures corresponding to SST variability than precipitation. Based on the correlation with MEI, runoff in the summer is also highly correlated with winter SSTs. Therefore, the anomalies in summer runoff are very likely integrated/accumulated results, as is also evident in the lag response to precipitation discussed in section 3.

SVD2$_r$ explains 16% of the total squared covariance. The SVD2$_s$ pattern (Fig. 13d) is similar to Fig. 12a, but with a few important differences. The Indian Ocean SST does not show organized anomalies as in Fig. 12a. In the western Pacific, the warm pool is not significant, but there is a strong cold center to the east of Japan. SVD2$_r$ has a dipole type of anomaly (Fig. 13e), with a southeast–northwest gradient, which has the negative anomaly covering the Huai He River basin and the area to the south of the CJR. The negative maximum is mainly over the southern tributaries of the CJR. The positive anomalies are located to the north of the CJR, with the maximum along the YR and Qin Ling Mountain areas. The correlation coefficient between runoff SVD2$_r$ and SST SVD2$_s$ is equal to 86%. The peaks of the SST are about 1-yr lags to the runoff. The temporal variations of PCs would produce negative anomalies in northern EC and positive anomalies in southern EC after 1965. Most interestingly, SVD$_r$ in Fig. 13 seems to split the linear trend in the SST/rainfall mode (Fig. 12) into two. SVD1 has the largest SST anomalies over the Indian Ocean and the western Pacific and deficit runoff over northern China. SVD2 has the strongest SST signal over the tropical eastern Pacific and western North Pacific and runoff anomalies over western, central, and southern China.

These modes indicate that the runoff in northern EC has a dry bias after the mid-1960s in response to the SST anomalies. The runoff over the areas to the south of the CJR is influenced by different SST modes, some of which may contribute to the flooding in that area. To more clearly visualize the overall effect of these modes, the JJA rainfall and JJA runoff differences based on observed data between 1966–80 and 1951–65 are shown in Figs. 14a and 14b, respectively. Both observed precipitation and runoff figures show dry anomalies in northern China, especially the Han Shui River basin, the Shandong Peninsula, Qin Ling Mountain, and the XJR basin. Figures also show wet anomalies in central and southwestern China, where two major southern tributaries of the CJR are located. The observed precipitation and runoff anomaly patterns are quite consistent, which again confirm that our interpolation methods are reasonable. For comparison, we reconstructed the precipitation and runoff differences between 1966–80 and 1951–65 based on first and second SVDs (Figs. 14c and 14d). The drought in northern EC and wet conditions over the CJR basin are evident in the figures. Furthermore, they are also consistent with the observed maps. In particular, the runoff SVDs almost reproduce the observed anomalies, which is an indication that the decadal variation of runoff over EC over that time period may well be influenced by the SST variations. However, for the precipitation, two SVDs apparently are not able to reproduce all precipitation anomaly patterns. Other factors likely contribute to rainfall anomalies.

Studies have shown that the nonuniqueness of the left and right singular vectors related to SVDs puts limitations on applications of the method (Newman and Sardeshmukh 1995; Hu 1997). Hu (1997) suggested that the SVD results can be used to assist us in gaining information about the correlation and covariance structure of two data series *after* their physical relation is known. By applying SVD in conjunction and consistent with real data analysis in this study, it is confirmed that the results discussed in this section are not an artifact of SVD analysis.

6. Summary and discussion

In this study, data from 72 runoff stations and 160 precipitation stations are employed to investigate the seasonal and interannual variability of runoff between 1951 and 1983 and its relationship with precipitation and SST. A methodology has been developed to apply the TRIP river network for spatial interpolation of runoff depth. The gridded runoff data have been checked and evaluated in this study and found to be generally consistent with the precipitation data and some published runoff maps at large scales. There is a clear seasonal variation in runoff that is consistent with the development of the East Asian summer monsoon. The lag response in runoff in several subregions in different seasons is also evident. The CJR and the YR appear to be boundaries to divide the runoff into different regimes. Nan Ling Mountain, Luoxiao Mountain, Qin Ling Mountain, and three tributaries of the CJR play important roles in producing/modulating the temporal variations and spatial distributions of the runoff in EC in this study.

Different spatiotemporal patterns of summer runoff and precipitation are investigated in this study using EOF and wavelet analyses. The analyses reveal interannual, biennial, quasi-6-yr, and longer-term variations in these patterns. The first runoff EOF mainly emphasizes the runoff over the CJR. The areas with maximum

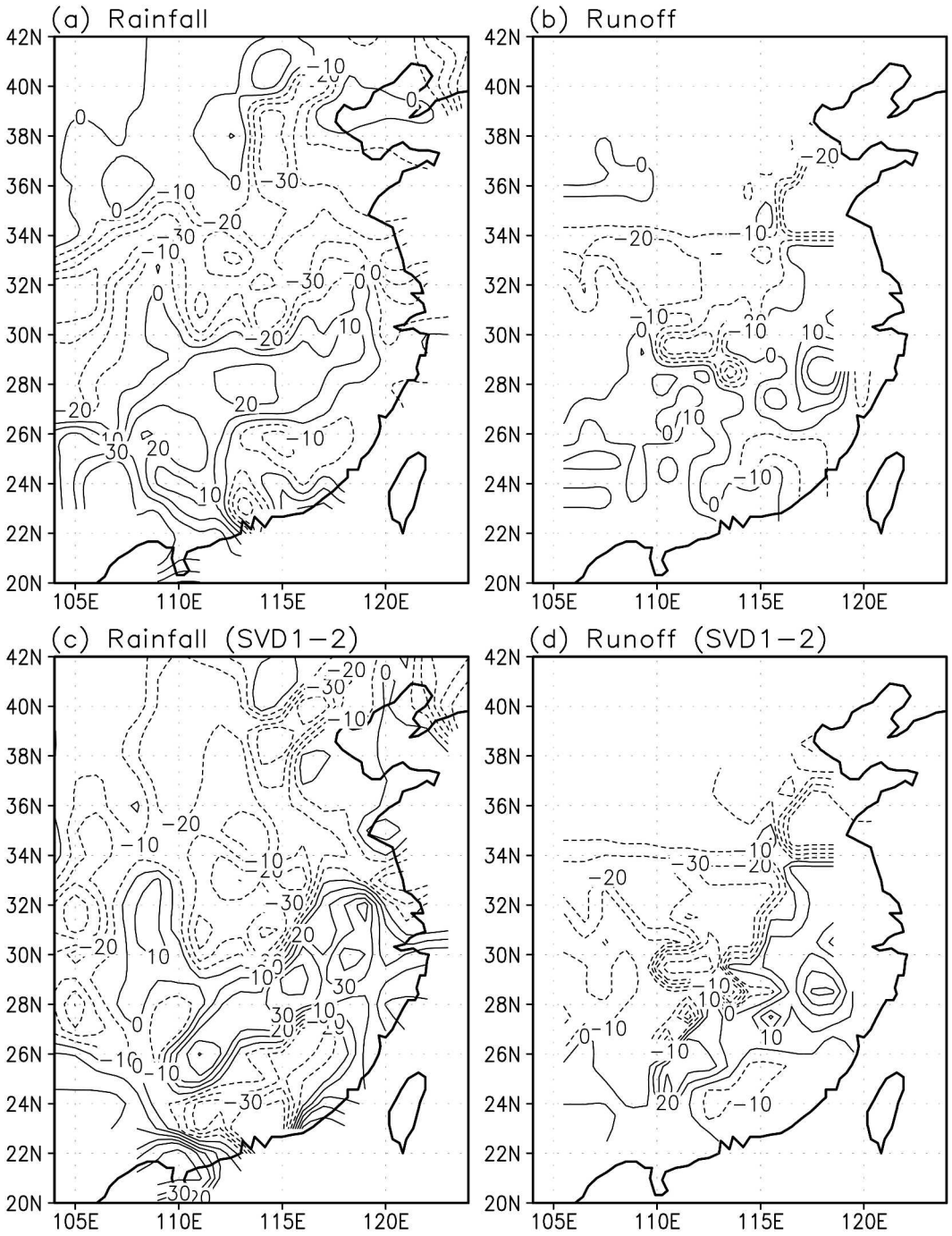

FIG. 14. Summer (JJA) rainfall and runoff difference between 1951–65 and 1966–80 (mm month^{-}). Based on (a) precipitation observation, (b) runoff observation, (c) precipitation SVD1 and SVD2, and (d) runoff SVD1 and SVD2.

EOF amplitude are located in two southern tributaries of the CJR, where the runoff has the largest standard deviation in this dataset. The areas with opposite sign are mainly located in the YR and the Hai He River with the maximum in the Shandong Peninsula, which has the largest CV in the dataset. The second EOF shows a dipole pattern with Nan Ling Mountain as the divider. The positive maximum is located in the XJR and the negative maximum is located in the Han Shui River. The PCs for runoff, EOF1$_r$, and EOF2$_r$, are highly cor-

related to the PCs for precipitation, $EOF2_p$, and $EOF1_p$, respectively.

Relationships between runoff and SST are investigated in this paper. The runoff's EOF PCs show significant correlation with one ENSO index (MEI) for the summer and the winter months, but precipitation PCs fail to show a significant relationship. By projecting EOF PCs onto SST, it is shown that dipole SST anomaly patterns in the western Pacific and the Indian Ocean's SST that are associated with El Niño underlie these runoff and precipitation EOFs. Furthermore, SVD analysis has also been conducted to investigate the interdecadal relationship between runoff and SST. It is interesting to notice that, instead of a heterogeneous spatial distribution of precipitation in SST/precipitation SVD analysis, the first runoff SVD shows a homogeneous response to the warm Indian Ocean and eastern Pacific, indicating that runoff over all of EC is very sensitive to climate change and responds to SST anomalies in one direction. A pronounced warm (SST) and dry (runoff) trend that is imposed on interdecadal variations in the PC has been identified. The second runoff SVD shows a dipole pattern with a southeast–northwest gradient. These SVDs are used to reconstruct a decadal anomaly pattern, showing more flooding in the CJR basin and dryness in northern China, mainly in the YR, consistent with observations.

It is likely that because of the cumulative nature of runoff, better separation of long-term SST-related signals is allowed compared to rainfall. Based on our result, one may now argue that the long-term drought trend in northern and northeastern China is a long-term signal, possibly related to the warming of the Indo-Pacific region, with linkage to global warming trends. On the other hand, long-term rainfall/runoff signals in central and southern China may be related to natural interdecadal variability. Notice that both PCs in Fig. 13 show an upward swing in the last two decades. The sandwich rainfall pattern (SVD1 of Fig. 12) is, therefore, a combination of two long-term signals, with different SST forcings and origins. These findings will have important implications in terms of causes of flood or long-term drought, as well as water resources in China.

Numerous studies have been conducted to investigate the mechanisms of different precipitation modes and precipitation–SST relationships in EC. The precipitation patterns have been linked to midlatitude circulation, Indian monsoons, SST anomalies, and land surface processes (i.e., Yatagai and Yasunari 1995; Xue 1996; Zhang et al. 1996; Lau and Weng 1999; WLX99; Xue et al. 2004). Further data analyses and model studies are necessary to verify the runoff modes and runoff/SST relationship that is discovered in this study and to understand the causes of these climate modes.

River runoff is highly subject to human intervention. Although this effect may not be a crucial factor on an annual basis, it could be vital on a shorter temporal scale. A correction to eliminate the human impact in the runoff data requires a tremendous amount of effort as well as necessary information, most of which resides in classified documents and is beyond our reach. In fact, because human intervention is so complex in EC, there is no guarantee this effect can ever be accurately corrected. Therefore, it is desirable to analyze the measured runoff and precipitation to see whether any meaningful results can be produced. In this study, by exhaustively comparing the gridded runoff and precipitation data and other data sources, we believe that our approach, especially the spatial interpolation of the runoff data, may be useful for the analysis of seasonal, interannual, and longer-term temporal and spatial variability of runoff and its relationship with precipitation and SST. We hope that this study will provide a useful resource for others interested in the large-scale hydrology of this region and stimulate more comprehensive data analyses and collection of runoff data for runoff, precipitation, and SST interaction studies in the future.

Acknowledgments. The authors thank Professor Dennis P. Lettenmaier for his support and help on this research, the Global Runoff Data Center (GRDC) for providing the runoff dataset, Prof. Longxun Chen of the Chinese Academy of Meteorological Sciences for the precipitation dataset, and Prof. Taikan Oki of the Tokyo University for the TRIP network. We also thank IAP for helping to collect the data and typing the hardcopy data to digital format, and Mr. Daniel Kahan for editing this paper. Funding was provided by NASA Grants NAG5-9014 and S-40416-G; NSF Grants EAR 9706403, ATM-0097260, and ATM-0353606; and Chinese CNSF Grants 40233034, 40075019, and KZCX2-SW-210.

REFERENCES

Chen, L., W. Zhu, and X. Zhou, 1998: Studies on climate change in China in recent 45 years. *Acta Meteor. Sin.,* **12,** 1–17.

Derbyshire, E., 1990: Environment: Understanding and transforming the physical environment. *Geography of Contemporary China*, T. Cannon and A. Jenkins, Eds., Routledge, 80–101.

Doty, B., cited 1995: The Grid Analysis and Display System (GrADS). User's guide. [Available online at http://grads.iges.org/grads/grads.html.]

Hu, Q., 1997: On the uniqueness of singular value decomposition in meteorological application. *J. Climate,* **10,** 1762–1766.

Hulme, M., 1992: A 1951–80 global land precipitation climatology

for the evaluation of General Circulation Models. *Climate Dyn.,* **7,** 57–72.

Institute of Chinese Water Resources and Electric Power, 1989: *Application of Chinese Water Resources* (in Chinese). Water Resource and Electric Power Publishing, 226 pp.

Kaylor, R. E., 1977: Filtering and decimation of digital time series. Institute of Physical Science and Technology, University of Maryland, College Park, Tech. Rep. BN 850, 14 pp.

Knutson, T., and S. Manabe, 1995: Time-mean response over the tropical Pacific to increased CO_2 in a coupled ocean-atmosphere model. *J. Climate,* **8,** 2181–2199.

——, and ——, 1998: Model assessment of decadal variability and trends in the tropical Pacific Ocean. *J. Climate,* **11,** 2273–2296.

Lau, K.-M., 1992: East-Asian summer monsoon rainfall variability and climate teleconnection. *J. Meteor. Soc. Japan,* **70,** 211–242.

——, and H. Weng, 1999: Interannual, decadal–interdecadal, and global warming signals in sea surface temperature during 1955–97. *J. Climate,* **12,** 1257–1267.

——, and ——, 2001: Coherent modes of global SST and summer rainfall over China: An assessment of the regional impacts of the 1997–98 El Niño. *J. Climate,* **14,** 1294–1308.

——, K.-M. Kim, and S. Yang, 2000: Dynamical and boundary forcing characteristics of regional components of the Asian summer monsoon. *J. Climate,* **13,** 2461–2482.

Lettenmaier, D. P., E. F. Wood, and J. R. Wallis, 1994: Hydro-climatological trends in the continental United States, 1948–88. *J. Climate,* **7,** 586–607.

Lins, H. F., 1985: Streamflow variability in the United States, 1931–78. *J. Climate Appl. Meteor.,* **24,** 463–471.

Maurer, E. P., A. W. Wood, J. C. Adam, and D. P. Lettenmaier, 2002: A long-term hydrologically based dataset of land surface fluxes and states for the conterminous United States. *J. Climate,* **15,** 3237–3251.

Newman, M., and P. D. Sardeshmukh, 1995: A caveat concerning singular value decomposition. *J. Climate,* **8,** 352–360.

Nickum, J. E., 1981: *Water Management Organization in the People's Republic of China*. M. E. Sharpe, Inc., 269 pp.

Nitta, T., and Z. Z. Hu, 1996: Summer climate variability in China and its association with 500 hPa height and tropical convection. *J. Meteor. Soc. Japan,* **74,** 425–445.

North, G. R., 1984: Empirical orthogonal functions and normal modes. *J. Atmos. Sci.,* **41,** 879–884.

——, T. Bell, R. F. Cahalan, and F. J. Moeng, 1982: Sampling errors in the estimation of empirical orthogonal functions. *Mon. Wea. Rev.,* **110,** 699–706.

Oki, T., and Y. C. Sud, 1998: Design of Total Runoff Integrating Pathways (TRIP)—A global river channel network. *Earth Interactions,* **2,** 1–36. [Available online at http://EarthInteractions.org.]

Parker, D. E., N. Y. Rayner, E. B. Horton, and C. K. Folland, 1999: Development of the Hadley Centre sea ice and sea surface temperature data sets (HadSST). *WMO Workshop on Advances in Marine Climatology-CLIMAR99,* Vancouver, BC, Canada, Environment Canada, 194–203.

Ropelewski, C. F., and M. S. Halpert, 1987: Global and regional scale precipitation patterns associated with the El Niño-Southern Oscillation. *Mon. Wea. Rev.,* **115,** 1606–1626.

Simmonds, I., D. Bi, and B. Yan, 1996: Relationships between summer rainfall over China and ocean temperatures in the tropical western Pacific. *J. Meteor. Soc. Japan,* **74,** 273–279.

Storch, H. V., and F. W. Zwiers, 1999: *Statistical Analysis in Climate Research*. Cambridge University Press, 484 pp.

Technique Team of Preliminary Products of National Water Research, 1981: The preliminary evaluation of Chinese water resources (in Chinese). The Office of Investigation and Division of Water Resources, the Ministry of Water Conservancy, 191 pp.

Torrence, C., and G. P. Compo, 1998: A practical guide to wavelet analysis. *Bull. Amer. Meteor. Soc.,* **79,** 61–78.

Trenberth, K. E., 1990: Recent observational interdecadal climate changes in the Northern Hemisphere. *Bull. Amer. Meteor. Soc.,* **71,** 988–993.

Wallace, J. M., C. Smith, and C. S. Bretherton, 1992: Singular value decomposition of wintertime sea surface temperature and 500-mb height anomalies. *J. Climate,* **5,** 561–576.

Wang, W.-C., and K. Li, 1990: Precipitation fluctuation over semi-arid region in northern China and the relationship with El Niño/Southern Oscillation. *J. Climate,* **3,** 769–783.

Weng, H.-Y., and K.-M. Lau, 1994: Wavelets, period doubling, and time-frequency localization with application to organization of convection over the tropical western Pacific. *J. Atmos. Sci.,* **51,** 2523–2543.

——, ——, and Y. K. Xue, 1999: Long term variations of summer rainfall over China and its possible link to global sea-surface temperature variability. *J. Meteor. Soc. Japan,* **77,** 845–857.

Wolter, K., and M. S. Timlin, 1993: Monitoring ENSO in LOADS with a seasonally adjusted principal component index. *Proc. 17th Climate Diagnostics Workshop,* Norman, OK, NOAA, 52–57.

——, and ——, 1998: Measuring the strength of ENSO events: How does 1997/98 rank? *Weather,* **53,** 315–324.

World Bank, 2001: *China: Air, Land, and Water*. The World Bank Press, 149 pp.

Xie, P., and P. A. Arkin, 1997: Global precipitation: A 17-year monthly analysis based on gauge observations, satellite estimates and numerical model outputs. *Bull. Amer. Meteor. Soc.,* **78,** 2539–2558.

Xu, S., 1990: *Chinese Synthesis Map Sets*. Chinese Map Publisher, 190 pp.

Xue, Y., 1996: The impact of desertification in the Mongolian and the Inner Mongolian grassland on the regional climate. *J. Climate,* **9,** 2173–2189.

——, H.-M. H. Juang, W. Li, S. Prince, R. DeFries, Y. Jiao, and R. Vasic, 2004: Role of land surface processes in monsoon development: East Asia and West Africa. *J. Geophys. Res.,* **109,** D03105, doi:10.1029/2003JD003556.

Yatagai, A., and T. Yasunari, 1994: Trends and decadal-scale fluctuations of surface air temperature and precipitation over China and Mongolia during the recent 40-year period (1951–1990). *J. Meteor. Soc. Japan,* **72,** 937–957.

——, and ——, 1995: Interannual variations of summer precipitation in the arid/semi-arid region in China and Mongolia. *J. Meteor. Soc. Japan,* **73,** 909–923.

Zhang, R., A. Sumi, and M. Kimoto, 1996: Impact of El Niño on the East Asian monsoon: A diagnostic study of the 86/87 and 91/92 events. *J. Meteor. Soc. Japan,* **74,** 49–62.

Zhang, Y., J. M. Wallace, and D. S. Battisti, 1997: ENSO-like interdecadal variability: 1900–93. *J. Climate,* **10,** 1004–1020.

Zhao, S., 1986: *Physical Geography of China*. John Wiley & Sons, 209 pp.